Supplementary Information for

Distinct roles of nuclear basket proteins in directing the passage of mRNA through the nuclear pore

Yichen Li,[1] Vasilisa Aksenova,[2] Mark Tingey,[1] Jingjie Yu,[1] Ping Ma,[1] Alexei Arnaoutov,[2] Shane Chen,[2] Mary Dasso,[2] and Weidong Yang[1*]

[1]Department of Biology, Temple University, Philadelphia, Pennsylvania, USA
[2]Eunice Kennedy Shriver National Institute of Child Health and Human Development, National Institutes of Health, Bethesda, Maryland, USA

* Correspondence: weidong.yang@temple.edu

List of Documents

Materials and Methods (additional)

Gene targeting with auxin-inducible degron. We used CRISPR/Cas9-tagged Nup153-NG-AID, AID-NG-Tpr, and Nup50-NG-AID cell lines published in Aksenova et al. study(1, 2). Following the same procedure we generated stable human cell line expressing Nup88 fused with NeonGreen fluorescent protein and auxin-inducible degron tags (AID tag), Nup88-NG-AID, for rapid degradation of Nup88 nucleoporin in DLD-1 cell line. In addition, we used Nup153-NG-AID, Nup50-NG-AID and AID-NG-Tpr TIR1- DLD-1 cell lines derived during the first step of nucleoporins tagging and described in Aksenova et al(1). To compare nucleoporins copy number in TIR1- and TIR1+ cell lines. All CRISPR/Cas9-tagged cell lines have been genotyped and tested for tagging and degradation by Western blot analysis, and immunofluorescence to prove that all copies Nup gene have been fused with NG and AID tag and degrade properly.

Cell culture. The human DLD-1 cell line was cultured in DMEM (Life Technologies) supplemented with 10% FBS (Atlanta Biologicals), antibiotics (100 IU/ml penicillin and 100 µg/ml streptomycin), and 2 mM GlutaMAX (Life Technologies) in 5% CO2 atmosphere at 37°C. Depletion of BSK-NUPs was achieved by the cultivation of cells in complete media, 5% CO2 atmosphere at 37°C in the presence of 1 mM auxin (Sigma Aldrich). Depletion time for nucleoporins in DLD-1 cell line: Nup153 – 60 min, Tpr –30 min, Nup50 – 90 min.

Western blotting. DLD-1 cells were lysed in 2x Laemmli Sample Buffer (Bio-Rad) directly on 12-well plates. Lysates were collected in eppendorf tubes and boiled for 15 min at 98°C, and ultra-centrifuged at 500 000g (TLA-120.1 rotor) for 10 min at 16°C. Protein samples were separated on 3-8% NuPaGE Tris-Acetate gels (Invitrogen) for 1 h and transfered onto PVDF membrane. The PVDF membrane was blocked in 5% non-fat milk for 1 h with the following incubation with the primary Tpr (A300-

828A, Bethyl), Nup153 (A301-789A, Bethyl), Nup50 (A301-782A, Bethyl) or Tubulin (T6199, Sigma-Aldrich) antibodies overnight at 4°C. Next, the membrane was rinsed three times in 1x TN buffer (150 mM NaCl, 1 mM TrisHCl, pH 7.5) and probed for 1 h with the secondary anti-mouse or anti-rabbit antibodies conjugated to HRP in 5% non-fat milk. Detection of the signal was performed using ChemiDoc Imaging System using SuperSignal WestPico PLUS Chemiluminescent Substrate (ThermoScientific). Tubulin and nucleoporins specific signal were obtained from the same PVDF membrane.

Immunofluorescence staining. Nup153-NG-AID, AID-NG-Tpr, and Nup50-NG-AID DLD-1 cell lines were seeded on 8-well Nunc Lab-Tek slides for two days. Then, cells were washed three times with 20 mM HEPES, pH 7.8; 2 mM DTT, 10% sucrose, 5 mM $MgCl_2$, 5 mM EGTA, 1% TX100, 0.075% SDS buffer with the following 4% paraformaldehyde fixation in PBS at RT for 10 min. Later, cells were blocked with 10% horse serum (Vector Laboratories) for 1 hour, and nucleoporin localization was detected by specific primary antibodies and Alexa Fluor-conjugated secondary antibodies (Invitrogen). The incubation time for primary and secondary antibodies was 2 hours and 45 min, respectively. The nuclei of fixed cells were visualized with Hoechst (Invitrogen). Images were acquired using Olympus UPlanSApo 100x/1.4 oil objective at Olympus IX71 inverted microscope (Olympus America Incorporation), equipped with an Ultraview spinning disk system (Ultraview ERS Rapid Confocal Imager; PerkinElmer) and controlled by Volocity software (PerkinElmer). Brightness and contrast were applied equally to all images using Fiji software version 2.0.0-rc-68/1.52e. RGB images from Fiji were processed to final resolution using Adobe Photoshop and Adobe Illustrator CS5.1.

Cell growth analysis. Survival of Nup153-NG-AID, AID-NG-Tpr, and Nup50-NG-AID DLD-1 cell lines after auxin treatment was analyzed(1, 2). Briefly, we imaged cells in brightfield or stained with crystal violet staining four days after auxin treatment. For crystal violet staining, cells were first

washed with PBS, then fixed with 70% ethanol for 15 min, and stained with 0.1% crystal violet for 15 min with the four following washes with the distilled water. Dried 96-well plates were imaged on the FluorChem Imaging System (ProteinSimple). Representative images are shown on Figure S2 b, d and f.

Plasmid and transport condition. Firefly Luciferase mRNA was extended by 24 MS2 stem loops on the 3′ end, and each loop was the binding target of an MS2-coating protein (MCP) dimer fused to mCherry. pMCP-mCherry, a plasmid bearing the open reading frame (ORF) of the MCP fused to mCherry and an SV-40 NLS, and pSL-MS2_24 ×, a plasmid bearing 24 copies of the MS2 stem loops, were received as generous gifts from Robert Singer (Albert Einstein College of Medicine). A Luciferase reporter plasmid bearing the MS2 stem loops was created in two steps. First, the ORF of IF2, PCR-amplified using a forward primer bearing SbfI and EcoRI restriction enzyme sites and a reverse primer bearing a NotI restriction enzyme site, was cloned into the corresponding SbfI and NotI sites in plasmid pmiR-GLO (Promega). Twenty-four copies of the MS2 stem loop from pSL-MS2_24 × were then cloned into the EcoRI–NotI restriction enzyme sites of the resultant plasmid, pmG-IF2, to generate pmG-MS2. Clones containing the MS2 stem loops were created in SURE2 bacterial cells (Stratagene) to minimize recombination of the MS2 repeats with the bacterial genome. Still, we had to resort to a two-step cloning procedure, as linearized plasmids containing the MS2 stem loops often recombined with the genome of competent bacterial cells, thus resulting in clones bearing smaller plasmids. The NLS was added to MCP to promote its import into the nucleus and enhance sufficient labelling of mRNAs even at the desired low MCP expression level. Freshly split DLD-1 cells were grown overnight on coverslips in DMEM (Grand Island, NY) supplemented with 10 mg ml−1 streptomycin, 100 U ml−1 penicillin and 10% newborn calf serum, at 37 °C, in a 5% CO2 incubator. Extensive control experiments showed each mRNP complex imaged in our experiments was tagged with ~8 mCherry molecules (Supplementary Fig. S7). Sequences of fluorescence images of mCherry were used to track mRNP export in living cells. Single-molecule

imaging and tracking experiments of the nuclear export of labelled mRNPs were conducted in living cells. Cells were washed with transport buffer (20 mM HEPES-KOH, 110 mM KOAc, 5 mM NaOAc, 2 mM $Mg(OAc)_2$ and 1 mM EGTA (pH 7.3)) for 30 mins before single-molecule imaging experiments in order to prevent autofluorescence from the culture media. Following imaging, the transport buffer is replaced with culture media and incubated for 24 hours and evaluated for healthy growth to ensure the health of the experimental cells.

Wide-field and narrow-field epi-fluorescence microscopy. Wide-field epifluorescence was performed using an Olympus IX81 equipped with a 1.4-NA 100× oil-immersion apochromatic objective (UPLSAPO 100×, Olympus), a 50mw 488nm semiconductor laser (Coherent OBIS), a 50mw 561nm laser (Coherent OBIS), and a Slidebook software package (Intelligent Imaging Innovations) for data acquisition and processing. NeonGreen and mCherry were excited by 488 and 561 nm lasers, respectively. Both green and red fluorescence emissions were collected by the same objective, filtered by a dichroic filter (Di01-R405/488/561/635-25 × 36; Semrock) and an emission filter (NF01-405/488/561/635-25 × 5.0; Semrock), and imaged by an identical Cascade 128+ CCD camera successively. Narrow-field epifluorescence microscopy was further realized by placing optical lenses with different focal lengthes on the beam path of excitation light, generating the illuminated area that ranges from 3 μm to 12 μm at the sample image plane as needed.

Laser scanning confocal microscopy. FV3000RS laser scanning confocal microscope (FV3000RS; Olympus, Shinjuku, Tokyo, Japan) was used for all our confocal microscopy experiments. The FV3000RS confocal microscope consists of Olympus IX83P2ZF equipped with a 1.4-NA 60X oil-immersion low chromatic aberration objective (PLAPON60XOSC2; Olympus, Shinjuku, Tokyo, Japan), 20-mW 488-nm continuous wave solid-state lasers (Coherent OBIS), Galvanometer Scanner with the scanning resolution from 64 x 64 to 4096 x 4096 pixels and scanning speed

from 2 μs - 1000 μs per pixels, single motorized pinhole with pinhole diameter of ø50–800 μm. a Cooled GaAsP photomultiplier, and the FV3000 system software (FV31S-SW; Olympus, Shinjuku, Tokyo, Japan) for data acquisition and processing. NeonGreen was excited by 488-nm laser. Live cells were scanned at the scanning resolution of 2048 x 2048 (104 nm/pixel) and 4096 x 4096 pixels (52 nm/pixels) respectively, and at scanning speed of 2 μs per speed. Cells were imaged while living and temperature was controlled to be 37°C.

High-speed single-molecule SPEED microscopy. High-speed single-molecule microscopy was performed with an Olympus IX81 equipped with a 1.4-NA 100× oil-immersion apochromatic objective (UPLSAPO 100×; Olympus, Shinjuku, Tokyo, Japan), a 50-mW 488-nm semiconductor laser (Coherent OBIS, Santa Clara, CA), a 50-mW 561-nm laser (Coherent OBIS), an on-chip multiplication gain CCD camera (Cascade 128+; Photometrics, Tucson, AZ), and the Slidebook software package (Intelligent Imaging Innovations, Denver, CO) for data acquisition and processing. An optical chopper (Newport) was used to generate an on–off mode of 561-nm laser excitation. NeonGreen and mCherry were excited by 488 and 561 nm lasers, respectively. To minimize alignment problems in dual-colour measurements, both green and red fluorescence emissions were collected by the same objective, filtered by a dichroic filter (Di01-R405/488/561/635-25 × 36; Semrock) and an emission filter (NF01-405/488/561/635-25 × 5.0; Semrock), and imaged by an identical Cascade 128+ CCD camera successively. Single molecules were detected at 2 ms per frame. The chromatic aberration between the red and green fluorescence channels was experimentally determined to be ~2-3 nm by measuring hundreds of Alexa Fluor-labeled GFP fluorescent molecules immobilized on the surface of the coverslip. A ~1 μm diameter circle area was illuminated at the focal plane during the experiment, and the illumination intensities at the focal plane were ~150 kW/cm^2 (488 and 561 nm).

RNA fluorescence in Situ hybridization (FISH). We quantified the number of firefly luciferase mRNA expressed in DLD-1 cells by Stellaris RNA FISH technique of LGC Biosearch Technologies. DLD-1 cells grew on coverslip were transfected with the plasmids of firefly Luciferase mRNA extended with 24xMS2 stem loops. We fixed DLD-1 cells with 3.7% Formaldehyde fixation solution (Sigma Aldrich) for 10 mins at room temperature and permeabilized cells with 70% (vol./vol.) ethanol (Sigma Aldrich) for 1hour at 4 °C. Hybridization was conducted by incubating fixed cells with Hybridization Buffer (LGC Biosearch Technologies) containing custom probe tagged with Quasar570 (LGC Biosearch Technologies) against firefly Luciferase mRNA at 37 °C for 16 hours. Finally, we counterstained nucleus of DLD-1 cells by incubating with 5 ng/mL DAPI (Sigma Aldrich) at 37 °C for 30 mins. In addition, we also conducted Stellaris RNA FISH for human transferrin receptor (TFRC) with TFRC probe tagged with Quasar570 (LGC Biosearch Technologies) as the control. The detailed proctocol of Stellaris RNA FISH technique of LGC Biosearch Technologies could be found at https://www.biosearchtech.com/support/resources/stellaris-protocols.

Following the FISH experiment, we proceeded to image samples with FV3000RS laser scanning confocal microscope. We used FV3000 system software for data acquisition and processing. Qusar570 and DAPI were excited by a 561-nm laser and a 405-nm laser respectively. Fixed cells were scanned in z dimension from the bottom to the top of a cell with a 250-nm z-step and the scanning region of 1024 pixel x 1024 pixel (208 nm/pixel) for each z-plane. Typically, a DLD1 cell can be sectioned into 40-48 z planes and an example of a single plane at equator of NE contains ~340 mRNAs was shown in Figure S8.

For post-imaging analysis, we utilized GDSC-SMLM plugin of ImageJ2/Fiji to fit each z-plane FISH image and obtained information including the spatial locations, the numbers, and the widths of single molecules. Then, we filtered single-molecule data based on the following criteria: 1) single molecules with the width that is smaller than 0.5 pixel are excluded because they cannot be

distinguished from background noise. And 2) if the localizations of two single molecules collected from two adjacent z-plane images are too close (< 25 nm), one of them is excluded as they might be collected from a same molecule appeared in both planes. Finally, we estimated the total number of mRNA molecules by summing up the number of single molecules collected from all z-planes. Averagely, ~ 12,000 mRNAs per cell and ~6,000 mRNAs per nucleus were determined.

Copy number of MCP-FPs per mRNP and mRNP size. To determine the copy number of MCP-FP molecules per mRNP, we quantified the fluorescence of a mCherry and mCherry-MCP-mRNP in vivo, each at the single-molecule level. As shown in Supplementary Fig. S7, each mRNP detected in our cell system has 7-8 copies of mCherry-MCP, which agrees well with previous reports in a similar MS2-mRNP cell system (3).The mRNA with the 24 MS2 loops has a length of ~3.3 kb (about 1.5 MDa), and each attached MCP-mCherry is 39 kDa. With multiple endogenous proteins bound to the mRNA, the final average mass of the mRNPs is estimated to be 4–5 MDa, with a corresponding diameter of up to ~25 nm when assuming a roughly spherical shape.

Localization of the NE The position of the NE was determined at subdiffraction limit accuracy by fitting the fluorescent or the bright-field images of NE. The pixel intensities within a row or a column approximately perpendicular to the NE were fit with a Gaussian. The peak position of the Gaussian for a particular set of pixel intensities was considered the NE position for that row and column. The peak positions of a series of such Gaussians were then fit with a second-degree polynomial, yielding the orientation of the NE within the entire image. The localization precision of the NE's middle plane is ~10 nm.

Localization precision of isolated fluorescent spots. The localization precision for fluorescent NPCs, as well as moving fluorescent mRNPs, was defined as how precisely the central point of each detected fluorescent diffraction-limited spot was determined. Fluorescent NPCs were fitted with a 2D elliptical Gaussian, and the localization precision was determined by the standard deviation

(s.d.) of multiple measurements of the central point. For moving molecules, the influence of particle motion during image acquisition should be considered in the determination of localization precision. In detail, the localization precision for moving substrates (σ) was determined by the equation

$$\sigma = \sqrt{F[\frac{16(s^2 + a^2/12)}{9N} + \frac{8\pi b^2 (s^2 + a^2/12)^2}{a^2 N^2}]}$$ where F is equal to 2, N is the number of collected photons, a is the effective pixel size of the detector, and b is the SD of the background in photons per pixel, and $s = \sqrt{s_0^2 + \frac{1}{3} D\Delta t}$, where s_0 is the SD of the point spread function in the focal plane, D is the diffusion coefficient of substrate, and Δt is the image acquisition time. Calculation of the diffusion coefficient was performed by plotting on a mean-square displacement versus time. The data was fitted with MSD=4DΔt.

The precision as obtained from the s.d. of multiple measurements and the above equation was verified by determining the localizations of immobile fluorescent molecules and fluorescent NPCs. A total of 230 immobile Alexa Fluor 647-labelled-GFP molecules were measured, and the two methods yielded a difference of 0.5±0.1 nm(3). In our measurements, typically millions of photons from 8- or 16-copies of NeonGreen fluorophores fused to 8- or 16-copies of Nups in an NPC were collected by using an optimized laser excitation power within 2-3 seconds. The collected millions of photons enabled us to achieve a spatial resolution of ~ 1-3nm and meanwhile the drifts of the NPC and the stage during the detection time of 3 seconds are negligible (< 1 nm). For individual 8-mCherry-labelled mRNPs, typically 2,500 signal photons versus 10 noise photons were collected from at a detection frame rate of 500 Hz in living cells. Correspondingly, the localization precision was ~12 nm for moving mRNPs on the basis of the above equations and the parameters determined experimentally (N > 2500, a = 240 nm, b ≈ 10, s_0 = 150 ± 50 nm, and D = ~ 0.14 μm^2/s for the

tested substrates). Noteworthy, the single-molecule localizations for mRNPs tracked in the NPC are the averaged positions since their real-time conformation and orientations are still unknown in the submicrometer NPCs due to technical limitations. Because of the inevitable vibration of NE of living cells, the localization precision of bright field NE or the NG-NPC centroid was ~10 and ~3 nm, respectively. Additionally, we used apochromatic 100x objectives in our microscope. The chromatic aberration between the red and green fluorescence channels was experimentally determined to be ~2-3 nm by measuring hundreds of Alexa Fluor-labeled GFP fluorescent molecules immobilized on the surface of the coverslip. Therefore, the overall tracking precision for mCherry-fused mRNP export through the NG-labelled NPC in living cells was estimated to be ~12–15 nm.

Determinations of NPC's centroid. Prior to recording single-molecule videos, the single NeonGreen-labeled NPC was imaged as a reference point for cells without the degradation of BSK-Nups, or the bright-field NE was imaged as a reference line for cells under the complete degradation of BSK-Nups. We typically completed the imaging of labeled NPC or NE within 1-2 seconds and the subsequent recording of single-molecule video within 20-30 seconds in a live cell. After single-molecule recordings, the image of the single NPC or the NE were collected again. By comparing the images taken before and after single-molecule recordings, drifts of the specimen stage and the objective during the short detection time were found negligible (typically < 5nm). If the drifting error is bigger than 10nm, the single-molecule recordings are discarded. By using the image for the NPC or the NE, the centroid of this NPC or the middle-plane of the NE were directly determined (detailed in the sections of "Localization of the NE" and "Localization precision of isolated fluorescent spots").

The above directly determined NPC's centroid or the middle-plane of the NE was firstly used to guide the plot of single-molecule tracking data within the NPC, and then was further verified or corrected after superposition of single-molecule localizations of transiting mRNP events in the NPC.

In detail, by fitting single-molecule localizations of mRNPs recorded in videos, the X and Y histograms for 2D spatial locations of mRNPs in individual NPC was obtained (**Supplementary Fig S12**). These histograms were fitted by Gaussian functions to obtain the single-molecule-based or indirectly determined NPC's centroid (detailed in the figure legend of Supplementary Fig S12). In this manuscript, we found that the resulting average shift between the image-based (directly determined)NPC centroid and the single-molecule-based (indirectly determined) NPC centroid is ~2-3 nm in the x dimension, and ~3-4 nm in the y dimension. Since the 2D-to-3D transformation algorithms were developed based on single-molecule localizations, the single-molecule-based (indirectly determined) NPC centroid was eventually used for determining the 3D nuclear export routes for mRNPs. This indirect determination of NPC centroid has been successfully verified and applied in our previous publications in spite of debate on this method(4-8).

Nuclear transport time of mRNPs is not affected by the absence of BSK Nups Although the export kinetics of mRNPs can be significantly altered by Tpr and Nup153, we found that the nuclear export time of mRNP was barely affected by the absence of any BSK Nups in our measurements. The nuclear transport time is mainly determined by two simple formulas ($R^2=nDt$ and $D=KT/6\pi\eta r$), in which R, n, D, t, K, T, η, and r are respectively traveling distance, dimension of movements, diffusion coefficient, transport time, K constant, environmental temperature, viscosity and molecular radius. As shown, the diffusion coefficients are proportional to temperature and inversely proportional to viscosity and radius. Absence of FG-Nups in nuclear basket doesn't change radius of NPC, viscosity of whole NPC and temperature of NPC, so that the diffusion coefficients of mRNA won't be largely influenced, which resulted in almost no changes in the nuclear export times for mRNPs.

2D to 3D transformation algorithm. An exhaustively detailed transformation process used to compute the 3D spatial probability density maps of particles transiting through the NPC was

described in our previous publications (8, 9) and demonstrated again here in Supplementary Fig S11-13. In short, the 3D spatial locations of molecules transiting through the NPC can be considered in either Cartesian (X, Y, Z) or cylindrical (X, R, Θ) coordinates. In microscopic imaging, the observed 2D spatial distribution of particle localizations are a projection of its actual 3D spatial locations onto the XY plane. The underlying 3D spatial distributions can be recovered by projection of the measured Cartesian (X, Y) coordinates back onto the simplified cylindrical (X, R, constant) coordinates, based on the expected cylindrically symmetrical distribution along the Θ direction of the nuclear pore. XY data is grouped into X dimensional bins 10nm or greater depending on the consistency of data along the X dimension and the number of data points collected along this axis. These XY data groupings are then utilized to calculate probability density maps representing the X and R dimensions the NPC. This is possible because for a radially symmetrical cylindrical geometry it does not matter whether imaging was performed from the XY (side view) or the YZ (radial cross section) plane. The obtained Y dimensional histograms are ideally identical. Thus from the data points collected along the axis of the NPC, the densities in the radial dimension can be obtained by solving the matrix equations provided in references (8, 9). More detailed information can be found in Supplementary Fig S14and its figure caption. The resulting 3D, surface-rendered visualizations shown in figures were generated with Amira 5.2 (Visage Imaging).

An estimated quantity of necessary data points required to resolve the pathway through the NPC as being either through the central axial channel, or the periphery of the NPC was calculated using Monte Carlo simulations. Simulations were conducted using randomly sampled X and Y positions confined to cylinders of varying radii corresponding to those obtained experimentally. Each sampled point was calculated using a probability distribution corresponding to our experimental single molecule localization precision to simulate error. The data was then run through (X,Y) to (X,R) transformation process. Thousands of iterations were run under the necessary conditions for each experiment to determine the minimum amount of data needed to

resolve a 3D spatial transport route with an acceptable reproducibility percentage. For the reproducibility percentage, the proportion of simulated data sets that fell within the acceptable range were calculated (See **Supplementary Fig S15 and Table S5**).

3D Route localization precision

To ensure a high reproducibility of 3D spatial probability density maps obtained for each membrane protein candidate, extensive measurements were conducted by combining experimental data and computational simulation. It is important to note that route localization precisions are different from single-molecule localization precision. In detail, the route localization precision is determined by two parameters: one is the number of single-molecule locations and the other is single-molecule localization precision. As shown in Supplementary Figure S15, simulated data was used to estimate the minimum number of single-molecule localizations required to generate a reliable 3D probability density map for routes of 25 nm (central channel transport) or 40 nm (peripheral channel transport) radial distances. A single-molecule localization precision of 10 nm was used to reflect the precision of our experimentally collected data. We used three different sample sizes (100, 200, and 500 points) and converted the 2D data to 3D by using our transformation algorithm. Peak positions were fitted for data generated from each of the three sample sizes. 100 fittings were used to determine the peak position and the standard deviation is used for the route localization precision. Simulation code can be found at: https://github.com/YangLab-Temple/Master.

3D Transport Route Reproducibility Simulation. The reproducibility of observed single-molecule data was validated through a Monte Carlo simulation previously developed by our lab group. This simulation utilizes the calculated localization precision of single-molecule localizations in conjunction with the quantity of experimentally derived single-molecule localizations to calculate the reproducibility of SPEED microscopy derived export routes. This simulation is open source and

can be found here: https://github.com/YangLab-Temple/Master/tree/master/reproducibility%20rate.

Alignments between different imaging approaches on the same light microscope. In some of our experiments, cell samples were subsequently imaged by wide-field transmission light and inverted beam-expanded or -focused lasers. Any misalignments between these different imaging modes were determined by comparing images of the same sample taken by these methods and later corrected in data analyses. In detail, first, we brought the equator of nuclear envelope (NE) to the focal plane under wide-field transmission light mode and took an image of NE. Then, we switched to wild-field, narrow-field or single-point fluorescence mode to image the same NE. Third, we localized the NE in both images and calculated any shifting errors. The errors were corrected in later data analyses.

Statistics. Experimental measurements are reported as mean ± standard error of the mean unless otherwise noted. A binomial z-test for proportions was utilized for efficiency assays. For generation of all 3D probability density maps, data from at least 8 cells was collected for each terminal for all FG-Nups. Specifically, the distribution of either the entrance frequency (entering vs. returning events) or the nuclear export efficiency (successful vs. abortive nuclear export events) follows a binomial function. Thus, the standard deviation (SD) of the distribution is calculated as SD= $\sqrt{\frac{p*(1-p)}{n}}$, n is the number of the total events; p is the percentage of the successful events and 1-p is the abortive events.

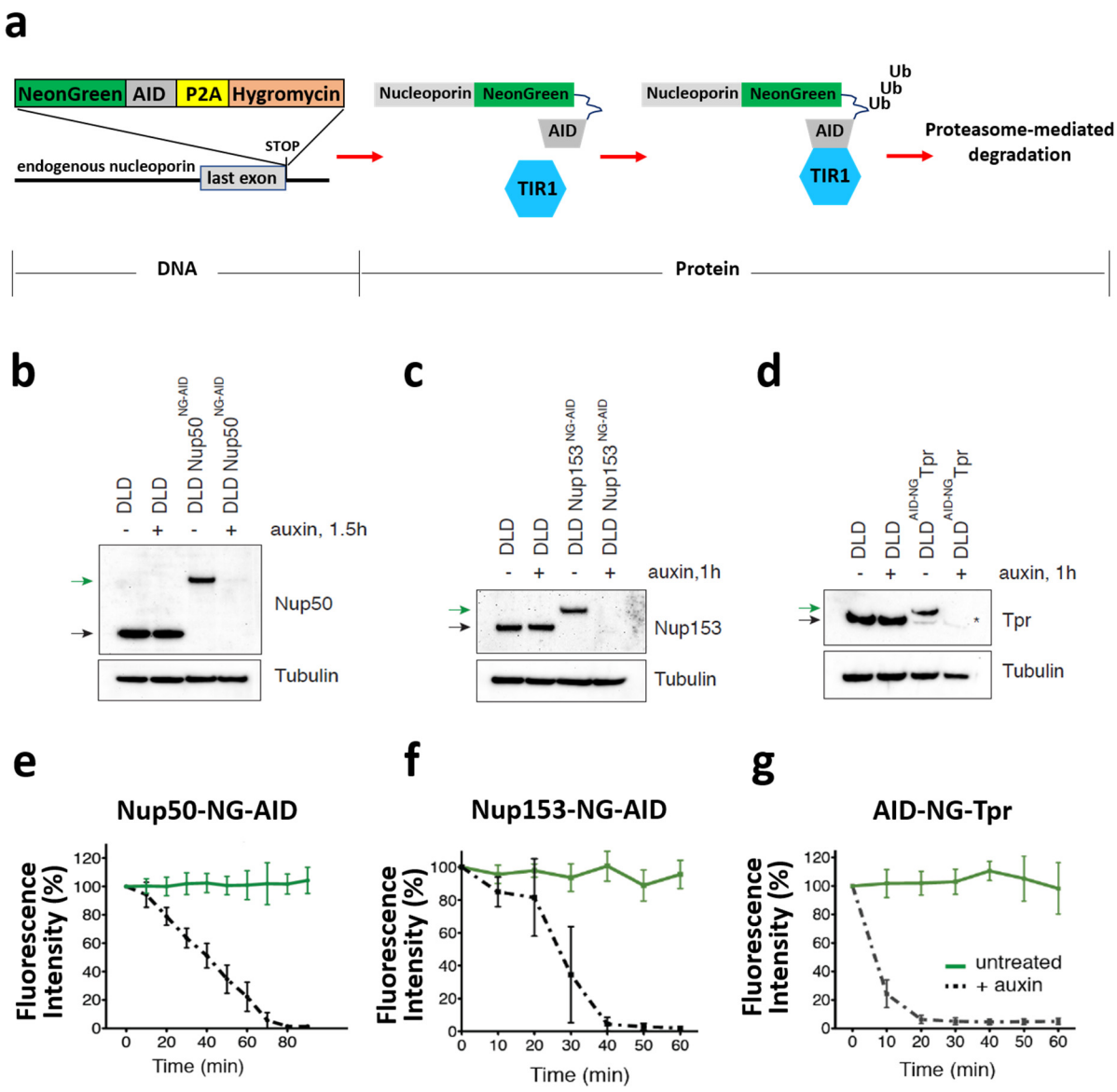

Supplementary Figure S1 Auxin-inducible rapid degradation (AID) strategy for nuclear basket nucleoporins (BSK-NUPs). **a**, The strategy of CRISPR/Cas9-based tagging of nucleoporin genes with AID sequence and degradation of the AID-fused nucleoporins. The TIR1 protein recognizes proteins tagged with AID domains upon the induction of the plant hormone auxin. This leads to their rapid conjugation with ubiquitin (Ub) and degradation. NeonGreen (NG) tag is used to count the copy number of BSK-NUPs. **b-d**, Western blot analysis for the degradation of Nup50, Nup153 and Tpr after 1-1.5 hours auxin treatment. Black and green arrows indicate the molecular weight of unmodified and NeonGreen-AID (NG-AID) tagged nucleoporins respectively. **e-g**, The fluorescence of NG-tagged Nup50, Nup153 and Tpr on the NE in the absence or presence of auxin.

Flueorescence intensity was recorded by the confocal microscope every 10 min over time of auxin-inducible degradation.

Supplementary Figure S1

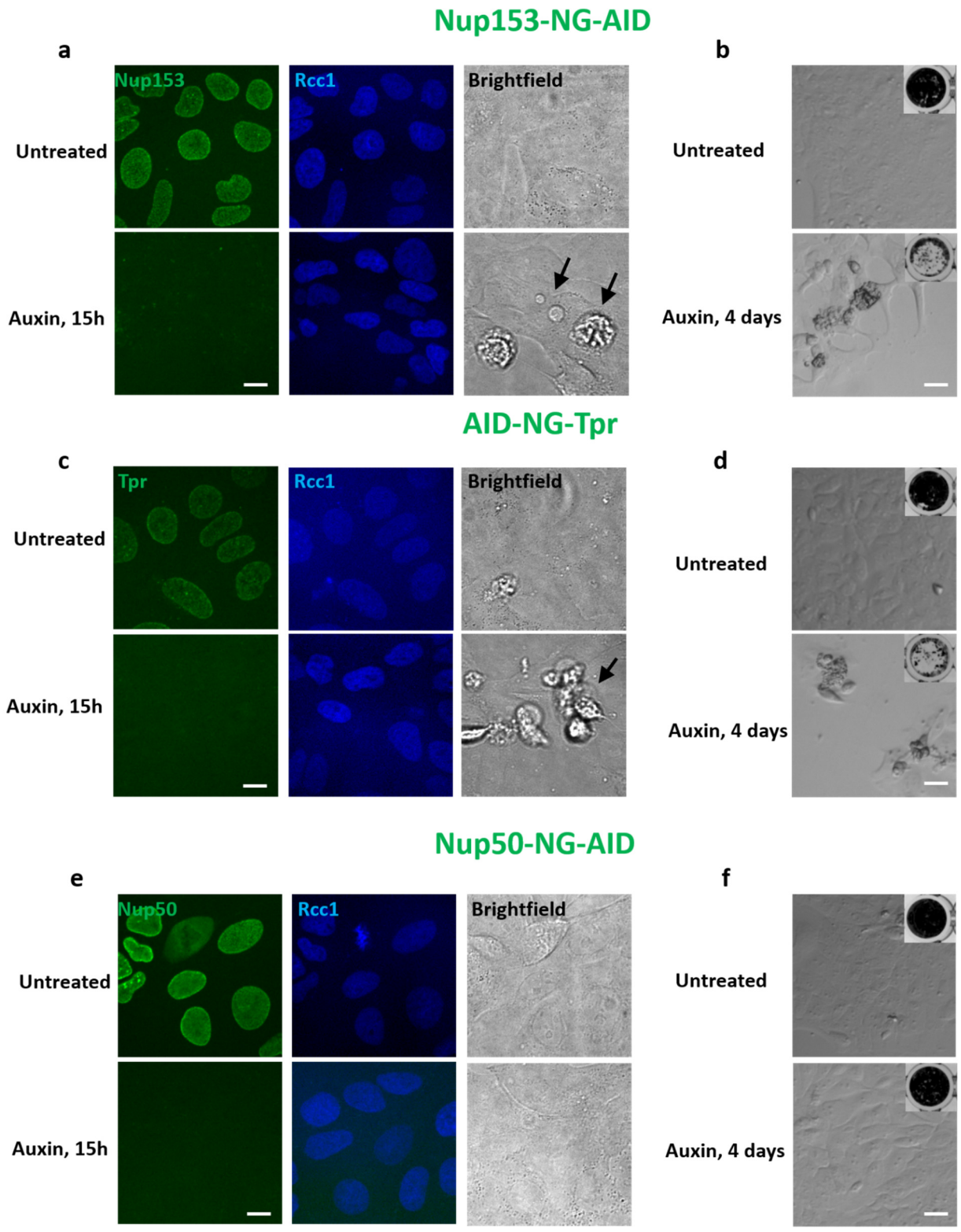

Supplementary Figure S2 Nup153 and Tpr nucleoporins are essential for cell viability. **a**, Live imaging of Nup153 degradation. Chromatin is visualized by RCC1 fluorescent protein (blue). Scale bar is 10 μm. The green fluorescence intensity at the nuclear envelope corresponds to tagged nucleoporins in the absence or 15 hours

treatment of auxin. In brightfield, the dying cells are pointed by black arrows. **b**, The confluency of Nup153-NG-AID DLD-1 cells in the absence or 4 days treatment of auxin. **c**, Live imaging of TPR degradation. The green fluorescence intensity at the nuclear envelope corresponds to tagged nucleoporins in the absence or 15 hours treatment of auxin. In brightfield, the dying cells are pointed by black arrows. **d**, The confluency of AID-NG-TPR DLD-1 cells in the absence or 4 days treatment of auxin. **e-f**, Live imaging of Nup50 degradation and the confluency of Nup50-NG-AID DLD-1 cells in the absence or 4 days treatment of auxin.

Supplementary Figure S2

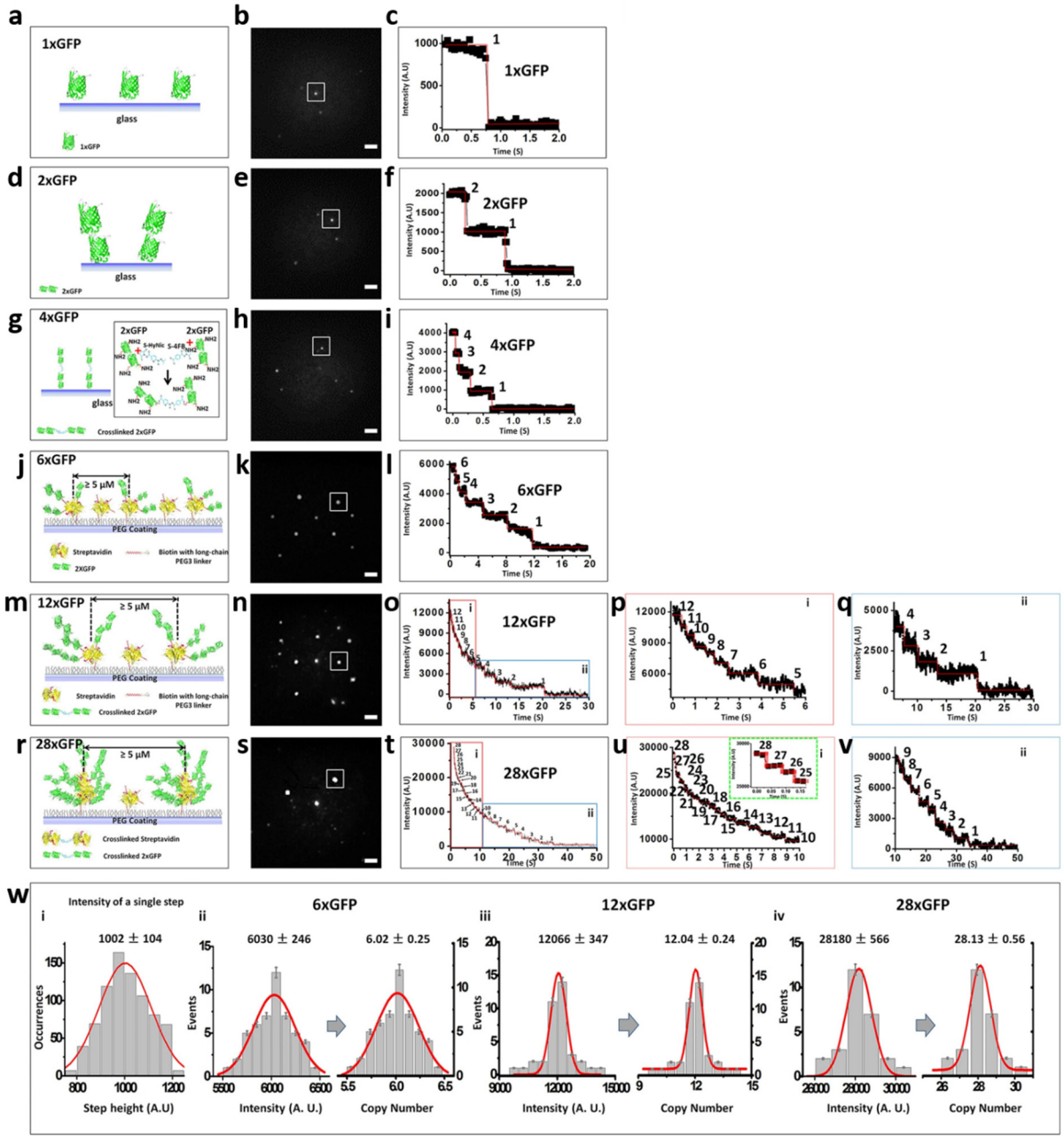

Supplementary Figure S3 Counting the number of GFP molecules in synthetic protein complexes using SPEED microscopy. **a**. Diagram shows 1xGFP anchored on the surface of coverslip. **b**. Wide-field epifluorescence images of 1xGFP. The fluorescent spot in the square was analyzed by SPEED microscopy; the spot generated the photobleaching curve shown in C. **c**. The photobleaching curve of a 1xGFP molecule. The black dots represent the fluorescent signal; the red line is the fitted

photobleaching steps; the number is the step count. **d-f**. The anchoring pattern, the epi-fluorescence image and the photobleaching curve of 2xGFP molecules. **g-i**. Construction and photobleaching analysis of 4xGFP molecules. **j**. Diagram shows the deposition of 6xGFP on the surface of coverslips. Scale bar: 5 μM. **k**. Wide-field epifluorescence images of 6xGFP on the surface of a coverslip. **l**. Photobleaching curves of 6xGFP molecules, showing six photobleaching steps were clearly resolved. **m-q**. Construction and photobleaching analysis of 12xGFP molecules. To have a detailed view, the photobleaching steps of a 12xGFP molecule were separated into red and green boxed areas, as shown in o, p and q. **r-v**. Construction, imaging and the photobleaching steps of a 28xGFP molecule. **w**. Intensity-based analyses of the copy number of GFPs in 6xGFP, 12xGFP and 28xGFP. (i) Distribution of intensities of single photobleaching steps collected from photobleaching curves of molecular complexes of GFPs (grey columns) fitted with a Gaussian function (red line). (ii–iv) Histograms (grey columns) fitted by Gaussian functions (red lines) show the distribution of initial intensities of photobleaching curves and the corresponding average copy numbers for 6xGFP, 12xGFP and 28xGFP constructs. The figure is reused with permission.

Supplementary Figure S3

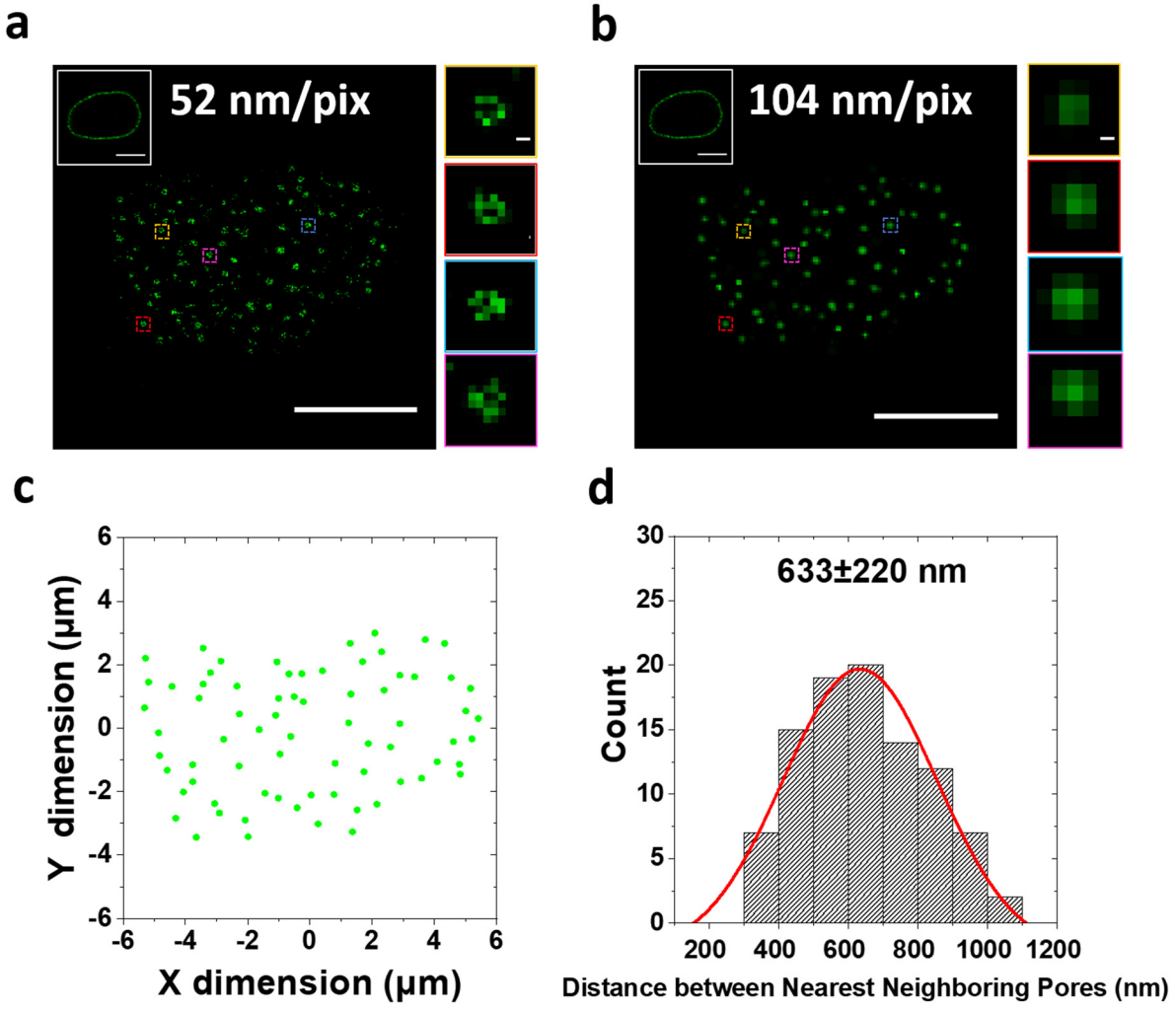

Supplementary Figure S4 Spatial density of NPCs at the bottom of NE in the DLD-1 cells. **a-b**, Typical confocal microscopy image of NG-NPCs (Nup153-NG) at the bottom of NE of DLD-1 cells shown with different pixel sizes. The equator of NG-NE was shown in the inset images, Bar 5μm. NG-NPCs selected in squares were further highlighted on the right sides, Bar 100 nm. **c**, Green spots corresponding to NG-NPCs in **b** were fitted by 2D Gaussian function to obtain the 2D centroids of these NG-NPCs. **d**, Distribution of the nearest neighboring-NPCs distances (d) for DLD-1 cells. The histogram was fitted with a Gaussian function (red line) to give the average distance of d=633±220 nm (mean±sd).

Supplementary Figure S4

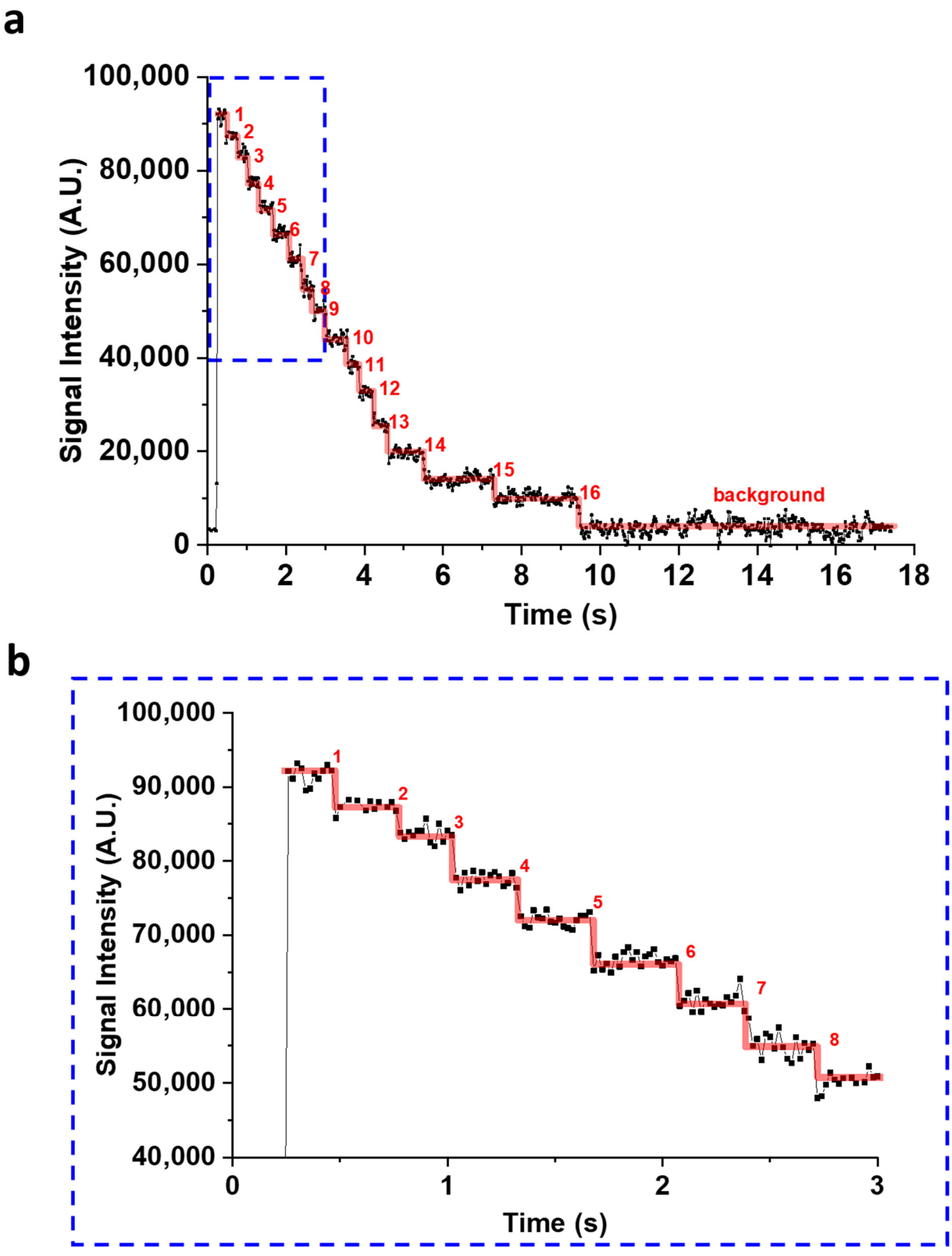
a
Signal Intensity (A.U.)
Time (s)
1
2
3
4
5
6
7
8
9
10
11
12
13
14
15
16
background
b
Signal Intensity (A.U.)
Time (s)
1
2
3
4
5
6
7
8

Supplementary Figure S5 Photobleaching curve for Nup88-NG. **a.** a typical photobleaching curve for a Nup88-NG labeled NPC in DLD-1 cells. Sixteen NG-fusion Nups photobleaching steps were resolved corresponding to sixteen copies of Nup88 per NPC. **b**. The first eight transient steps were enlarged.

Supplementary Figure S5

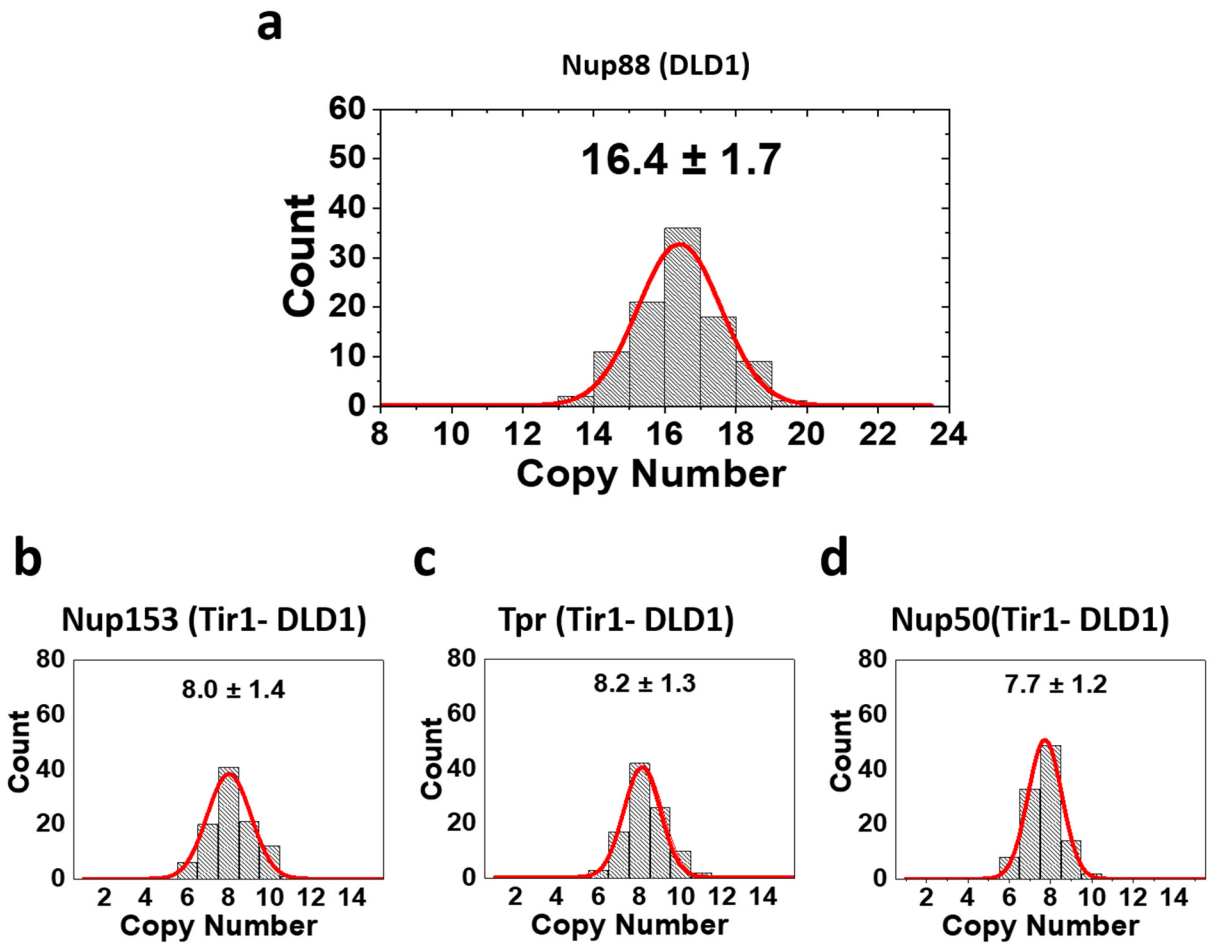

Supplementary Figure S6 The copy number of nucleoporins (Nups) counted by widefield epi-fluorescent microscopy. **a.** Histograms of copy numbers of NG-labelling scaffold Nup per DLD-1 cells' NPC achieved from the initial intensities per NG-NPC divided by the intensity of a single Nups-NG molecule. Gaussian fittings (red line) of the histograms yielded averaged copies for Nup88 per DLD-1 NPC. **b-d**. Histograms of the copy numbers of NG-labelling BSK-Nup per Tir1- DLD-1 cells' NPC achieved from the initial intensities per NG-NPC divided by the intensity of a single Nups-NG molecule. Gaussian fittings (red line) of the histograms yielded averaged copies for three BSK-Nups per NPC of Tir1- DLD-1 cell.

Supplementary Figure S6

a

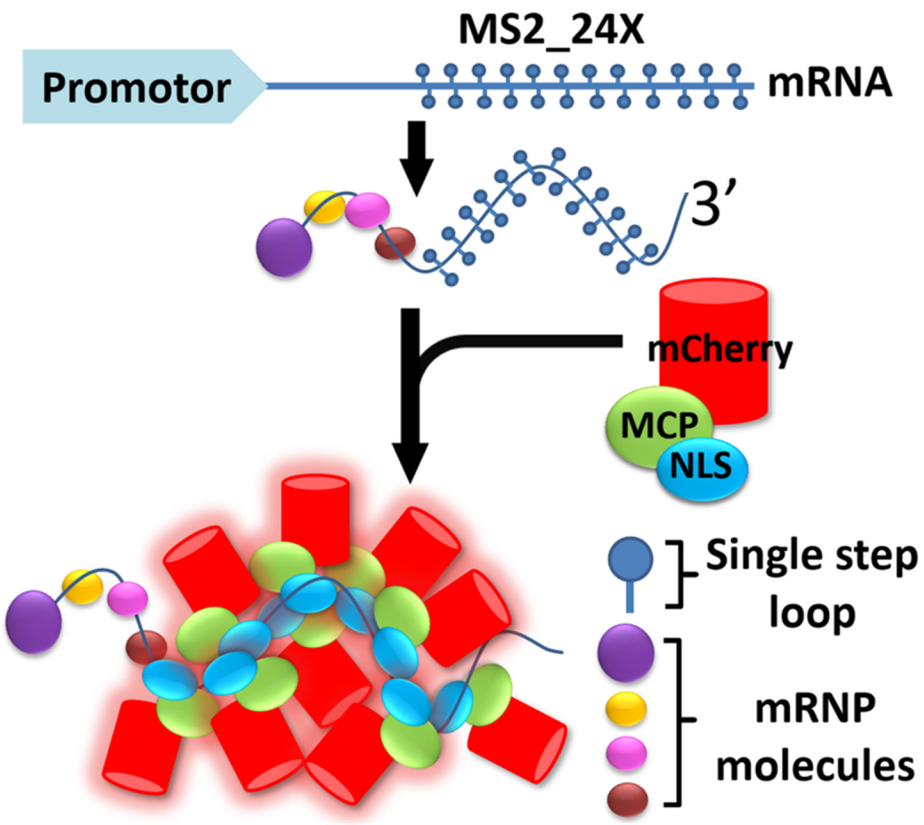
MS2_24X
Promotor
mRNA
3'
mCherry
MCP
NLS
Single step loop
mRNP molecules

b

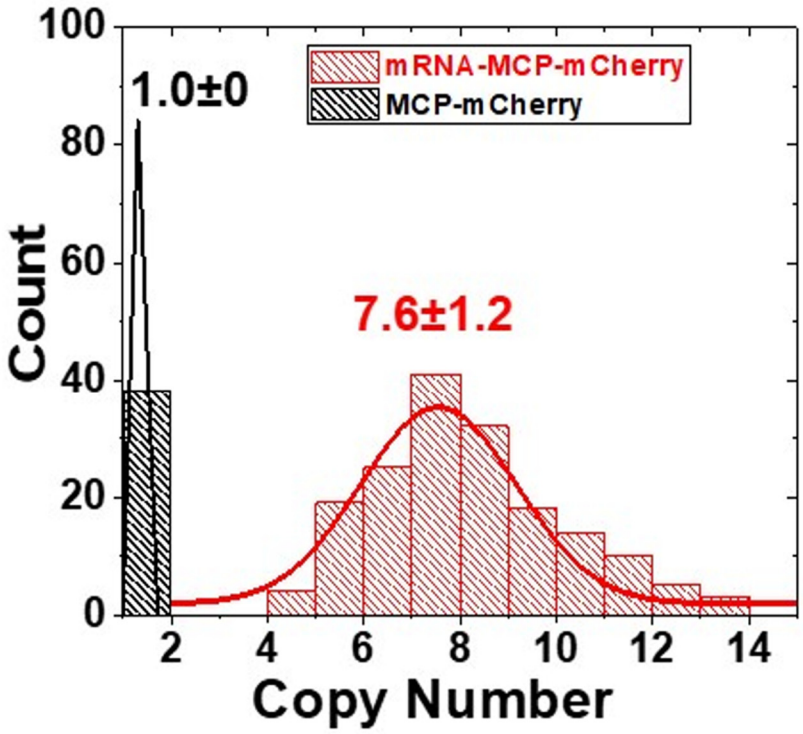
mRNA-MCP-mCherry
MCP-mCherry
1.0±0
7.6±1.2
Count
Copy Number
0
20
40
60
80
100
2
4
6
8
10
12
14

Supplementary Figure S7 Labeling strategy for mRNA and numbers of mCherry labeled per mRNA. **a**. pmG-MS2 with 24 MS2 stem loops at the 3' endings. mRNP with MS2_24X formed and is further recognized by mCherry-MCP-NLS. **b**. Comparisons between the intensities of single mCherry and single mCherry-tagged mRNP fitted with Gaussian functions (red curve) revealing that there are ~8 copies of MCP-mCherry per mRNP.

Supplementary Figure S7

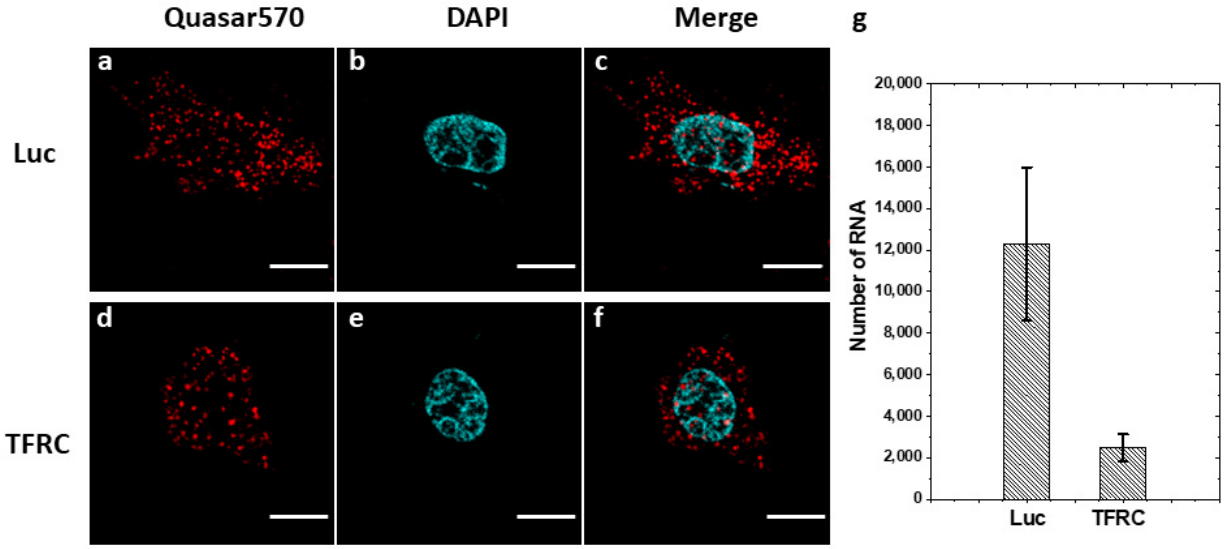

Supplementary Figure S8. RNA FISH of Luciferase mRNA in DLD-1 cells. a-c, RNA FISH for luciferase (Luc) mRNA in DLD-1 cells detected by custom probe tagged with Quasar570. Quasar570 fluorescence (a); DAPI (b), Merge of Quasar570 and DAPI (c) at the focal plane of equator of NE. Bar:5 μm. **d-f,** mRNA FISH for human transferrin receptor protein (TFRC) mRNA detected by the probe tagged with Quasar570. Quasar570 fluorescence (d), DAPI (e), Merge of Quasar570 and DAPI (f) at the focal plane of equator of NE. Bar:5 μm. **g,** The number of mRNA per whole DLD-1 cell for luciferase mRNA and TFRC mRNA, which were collected from 10 cells respectively. The detailed number of mRNAs in the nucleus and cytoplasm of cells is shown in **supplementary table 6**.

Supplementary Figure S8

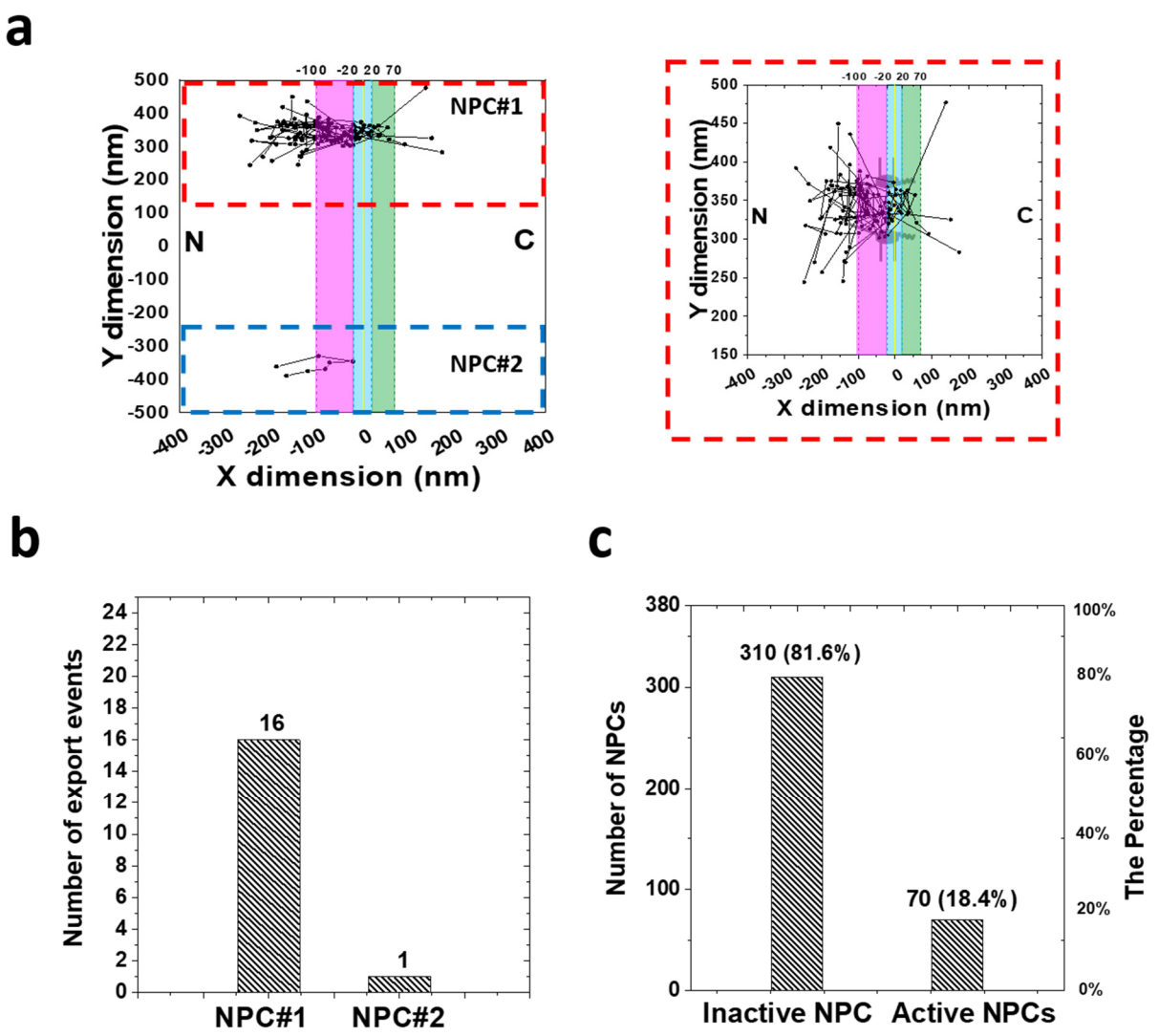

Supplementary Figure S9 Two NPCs possess different active statuses in medicating the nuclear export of mRNPs. a. Single molecular trajectories of mRNPs superimposed with a potion of the NE in a DLD-1 cell. Sixteen single-molecule trajectories clusted at the position of NPC#1 (red dash-line square, enlarged for a clear look on the right) and only one single-molecule trajectory was found at NPC#2 (blue dash-line square) within the same detection time. The middle-plane of the NE (yellow line at 0 nm), the nuclear basket (pink region between -100 nm and -20 nm), the central scaffold (region between -20 nm and 20 nm) and the cytoplasmic fibril (green area from 20 nm to 70 nm) are marked in the figure. NE, nuclear envelop; C, cytoplasm; N, nucleus. **b.** The number of mRNPs export events occurring in the two NPCs recorded within 20 seconds. **c.** The number and percentage of active and inactive NPCs observed from DLD1 cells with integrate

NPCs and Nups-depleted NPCs.

Supplementary Figure S9

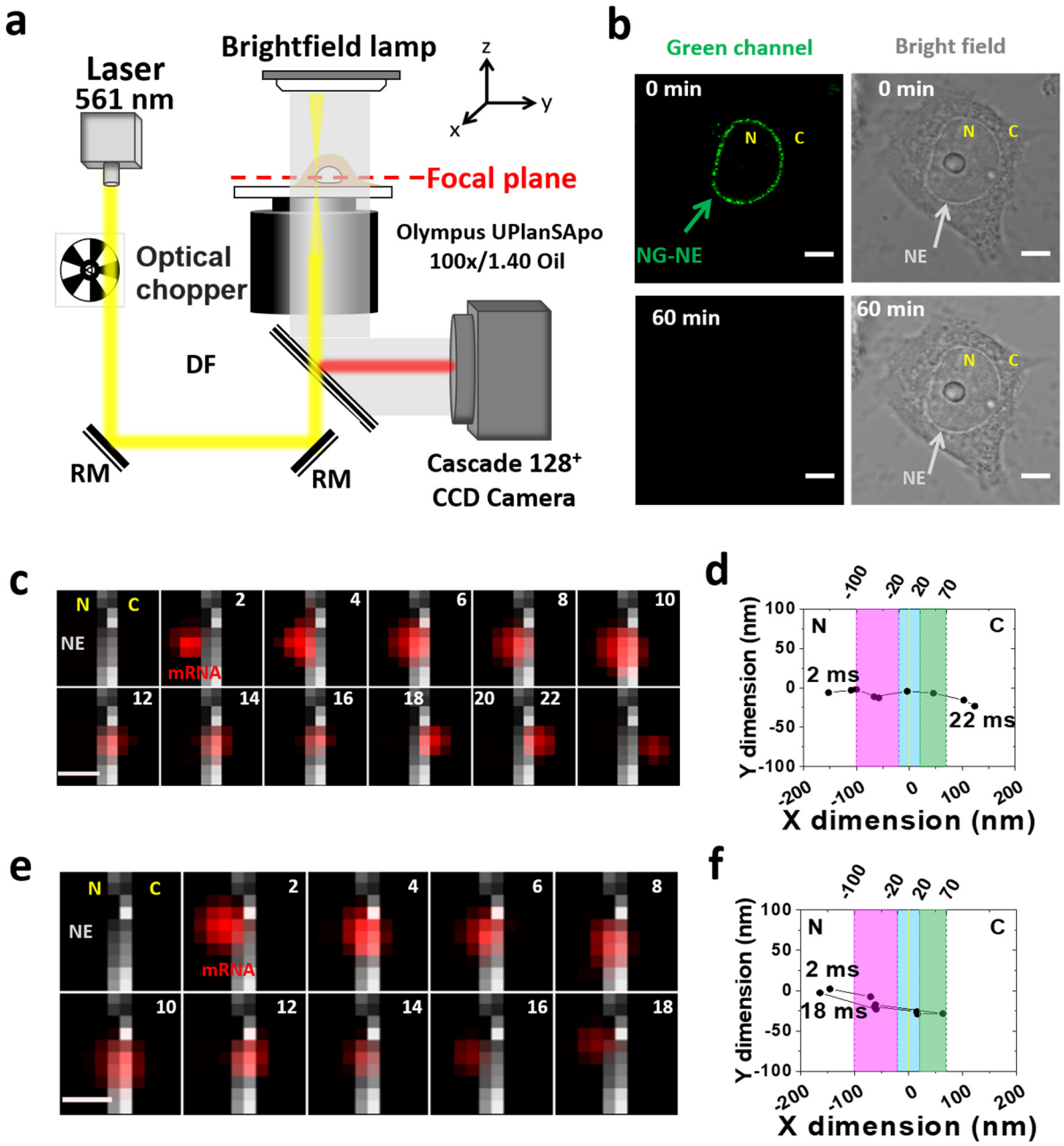

Supplementary Figure S10 Nuclear export of mRNA under thorough degradation of FG-Nups tracked by high-speed super resolution microscopy. **a**. Optical schematic of the high-speed super-resolution microscope. The brightfield lamp was utilized to illuminate NE at the equatorial plane of a DLD-1 cell nucleus in the focal plane. The 561 nm laser was chopped by an optical chopper to achieve an on-off laser mode with a laser-on time of 60 ms and a laser-off time of 140 ms. The longer laser-off time gives particles transiting the NPC

sufficient time to escape from the illumination volume and for fresh fluorescent cargo to diffuse from the nucleus into the NPC. **b**. The thorough degradation of Nup153-NG after 60-min auxin treatment. Bar 5μm. **c**. A typical successful single mRNP export event captured by high-speed super-resolution microscopy. A single mCherry-tagged mRNP (red spot) started from the nucleus, interacted with NE (gray line) and arrived in the cytoplasm. Numbers denote time in milliseconds. Bar 1μm. **d**. Corresponding Single-particle tracks (black dots) were acquired by 2D Gaussian fitting to point spread functions in a series of images for the successful event in **c**. The midline of NE (yellow line) was localized by bright-field imaging of NE in **c** (method). We arbitrarily defined axial length of nuclear basket, central scaffold and cytoplasmic fibril as 80 nm, 40 nm and 50 nm respectively, based on NPC scaffold structure attain from EM study. pink region (nuclear basket), light blue region (central scaffold) and light green region (cytoplasmic fibril). **e**. A typical abortive single mRNP export event. A single mCherry-tagged mRNP (red spot) started from nucleus, interacted with NE (gray line) and returned to the nucleus. Numbers denote time in milliseconds. Bar 1μm. **f**. Corresponding single-particle tracks (black dots) were acquired via 2D Gaussian fitting to point spread functions in a series of images for the abortive event in **e**. NE, nuclear envelope; C, cytoplasm; N, nucleus.

Supplementary Figure S10

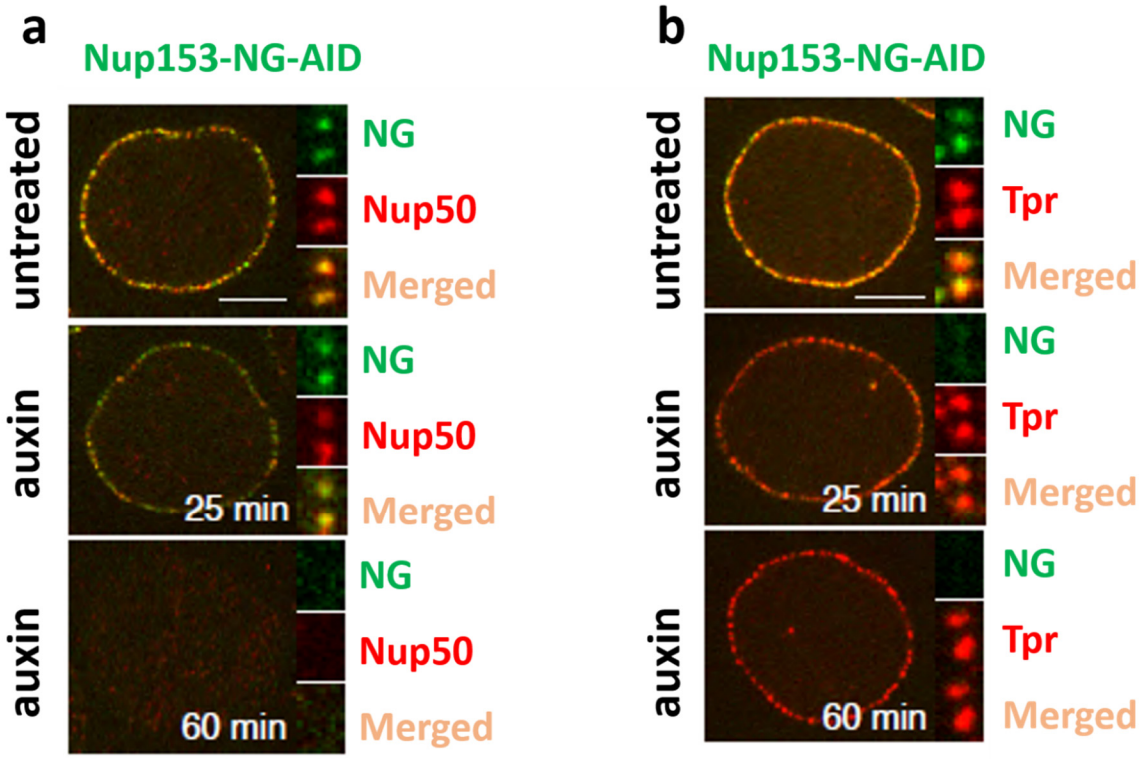

Supplementary Figure S11 Loss of Nup153 impairs localization of Nup50 but not TPR. **a**. One hour degradation of Nup153 mislocalizes Nup50, while Nup50 still localizes on the NE after 25 min of degradation. Scale bar, 5 μm. **b**. The Tpr localization at the NE is independent of Nup153. Scale bar, 5 μm.

Supplementary Figure S11

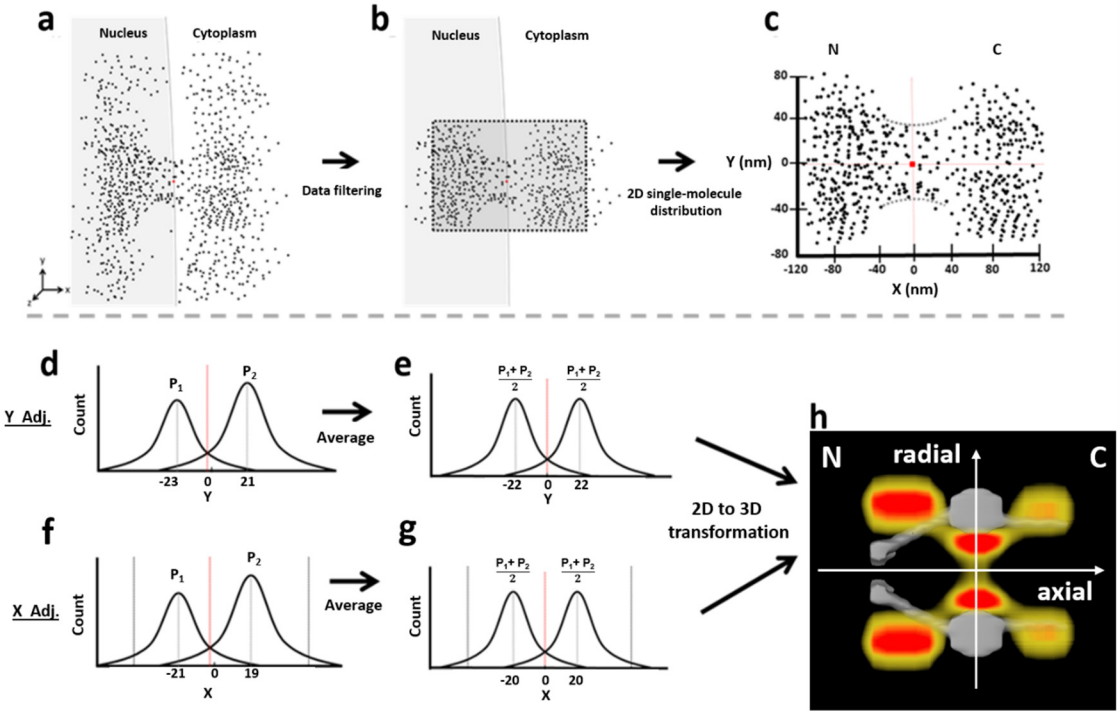

Supplementary Figure S12 Determination of the central axis of the NPC. **a.** The single-molecule tracking data (black points) are plotted around the initially determined NPC's centroid. **b.** The collected data after filtering by using single-molecule spatial localization precision. **c.** The filtered 2D single-molecule data shape the spatial location of the NE and a single NPC. The red dot represents the location of the NPC's marker. But sometimes the marker's position is not perfectly overlapped with the averaged central positions in either x or y dimension suggested by the 2D single-molecule data. Also, the 2D single-molecule distribution also indicates the orientation of NPC. If the orientation of the NPC is within a free angle of 1.4° to the perpendicular direction to the NE, the 2D single-molecule data will be proceeded further. If the point is outside of the selected region, then point will be dropped. **d.** The plot of projected locations of these 2D single-molecule data in the y dimension will indicate if a fine adjustment for the central cytoplasmic transport axis is needed or not. Here we just show an example that peak 1 (p1) and peak 2 (p2) are not symmetrical locating at -23 nm and 21 nm respectively. If the peaks are symmetrical, the step E will be skipped to move onto the 2D to 3D transformation directly. **e.** The two peaks are averaged as ((p1 + p2)/2), resulting a fine adjustment in the NPC will indiccytoplasmic transport axis. The dotted red line has shifted to the corrected central position. **f-g.** Similar to the y-dimensional data process, we next determine the precise location of the NPC's central position along the x dimension by fitting

the histogram of these 2D single-molecule locations within the NPC's scaffold region projected into the x dimension (ranging from -20nm to 20nm, as clearly shown in the void region of the NE in **c** even if the NPCy-dimensional data process, we next d**h.** The 2D single-molecule data with the confirmed x and y axes will undergo the 2D to 3D transformation (Fig. S10) to produce the 3D density map of mRNPs (red clouds). C: cytoplasm; N: nucleus. The figure was adapted from our previous publication with permission(8).

Supplementary Figure S12

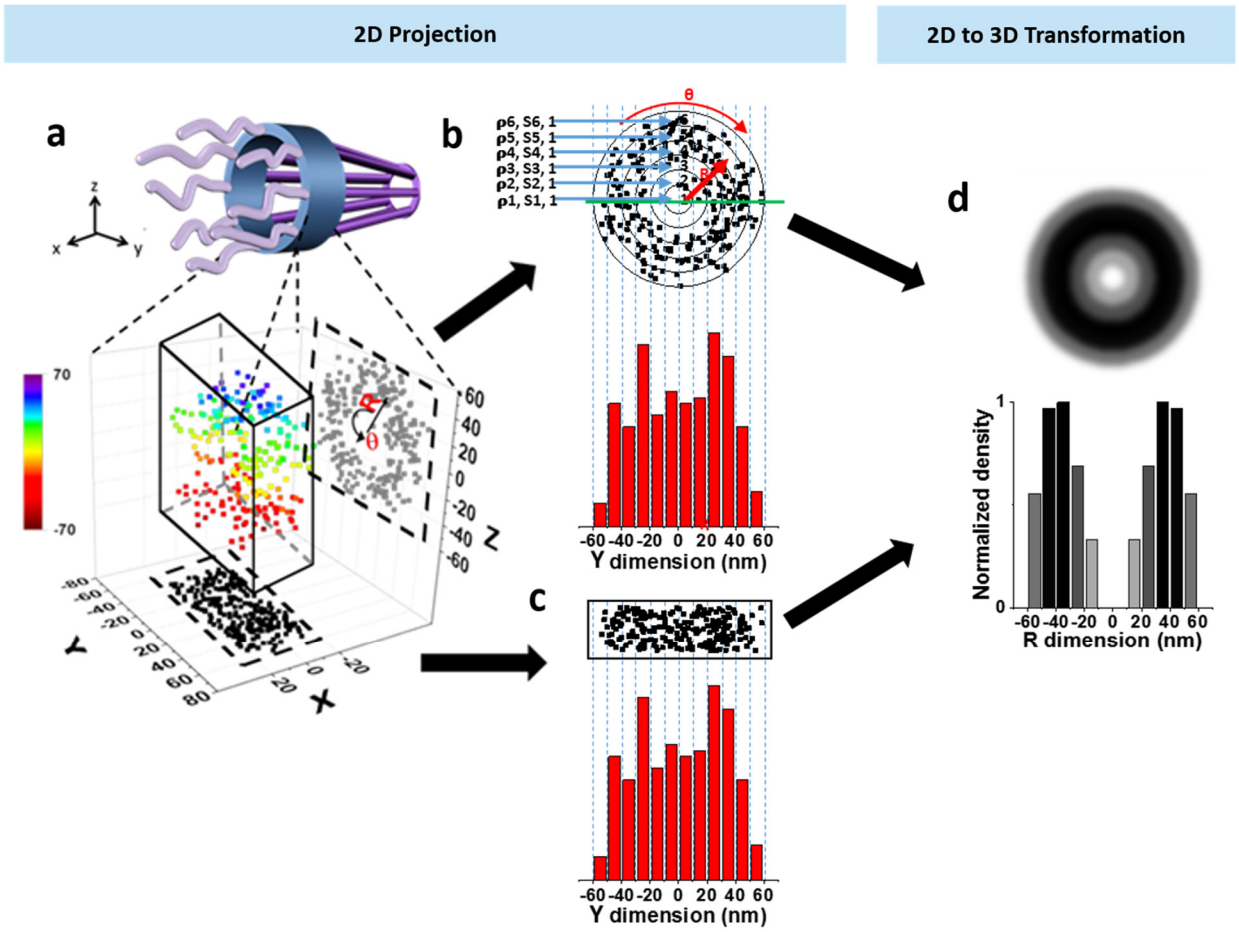

Supplementary Figure S13 A schematic demonstration, with simulated data, of the 2D to 3D transformation algorithms for molecules that diffuse through the NPC. **a.** 3D spatial locations of randomly diffusing molecules inside the NPC can be coordinated in a cylindrical coordination system (R, Θ, Y) due to the cylindrical rotational symmetry of the NPC. The 3D molecular locations in the NPC (rainbow colored for Z position) are projected onto a 2D plane in a Cartesian coordination system (X and Y, shown as black points) by microscopy imaging (Y and Z shown as gray points). **b.** The cross-sectional view of all the locations shown in **a** (same as the gray points from the Y and Z dimension). These locations can be grouped into the sub-regions between concentric rings. Given the high number of randomly distributed molecules in the NPC the spatial density of locations (ρ_i) in each sub-region ($S_{(i,j)}$) between two neighboring rings will be rotationally symmetrical and uniform. These locations can be further projected into 1D along the Y dimension. The locations along Y dimension can be clustered in a histogram with j columns. The total number of locations in each column

($A_{(i,j)}$) is equal to $2 * \sum_{i=j}^{n} \rho_i * s_{(i,j)}$, which is further explained in Figure S9. **c.** Histograms of 2D projected data from microscopy experiments are identical to **b**, thereby allowing us to use the aforementioned formula to determine the density of each concentric ring. **d.** Using the algorithms, 2D projected data can be used to reconstruct the 3D spatial distribution of protein location on the NPC. The figure was adapted from our previous publication with permission(8).

Supplementary Figure S13

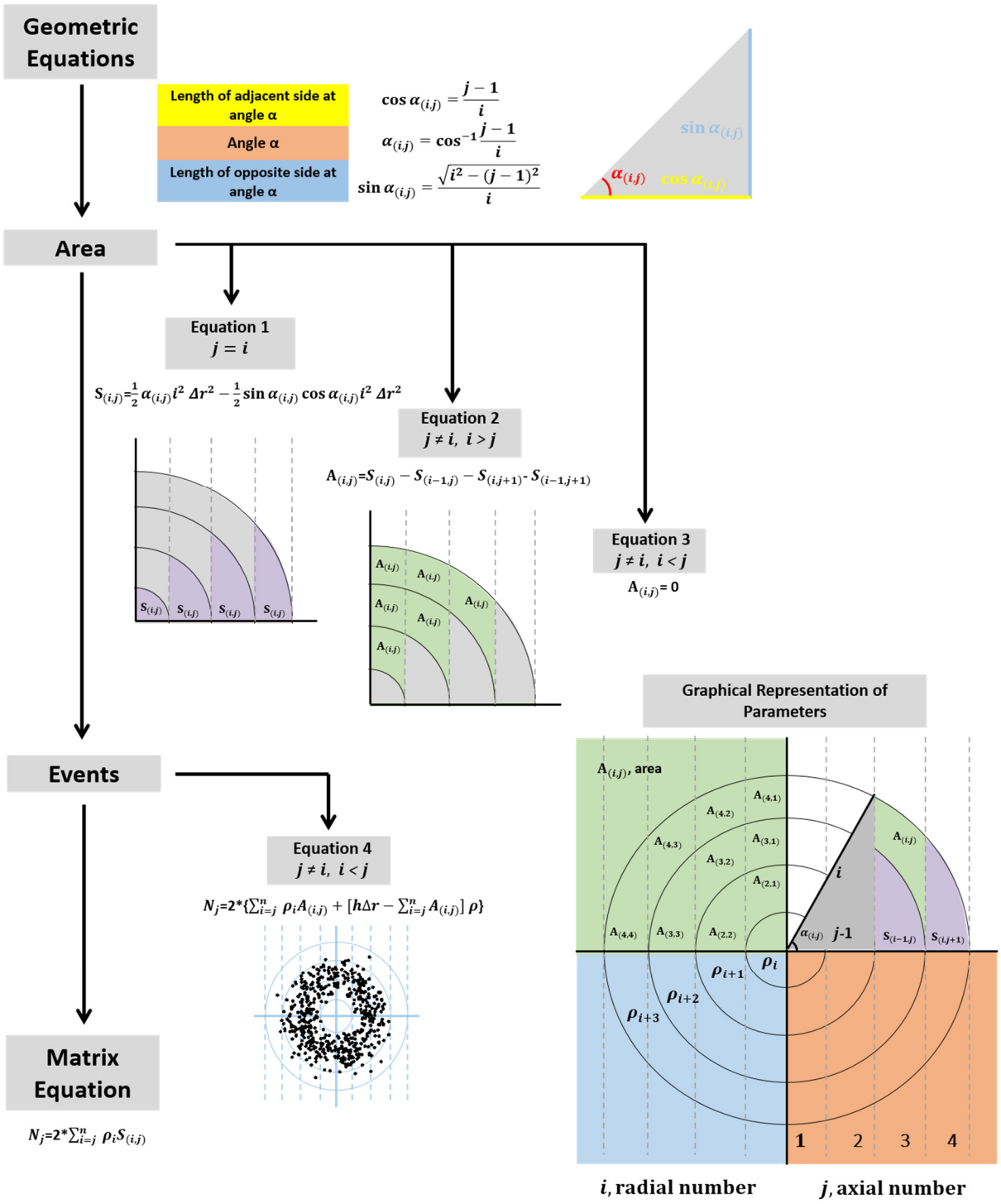

Supplementary Figure S14 Matrix equation flowchart. ($A_{(i,j)}$), area of the sub-region, (i), radial number, (j), axial number, (ρ_i), spatial probability density in each radial ring, ($S_{(i,j)}$), area of the sub-region, (N_j), number of events, and (Δr), bin size. Equations 1 – 3 will determine the area of the sub-region given certain

parameters (i.e. i = j). Equation 4 will determine the number of events in the given area. Once the subregion area ($A_{(i,j)}$) and events (N_j) are known, the spatial probability density in each radial ring (ρ_i) can be calculated. The figure was adapted from our previous publication with permission(8).

Supplementary Figure S14

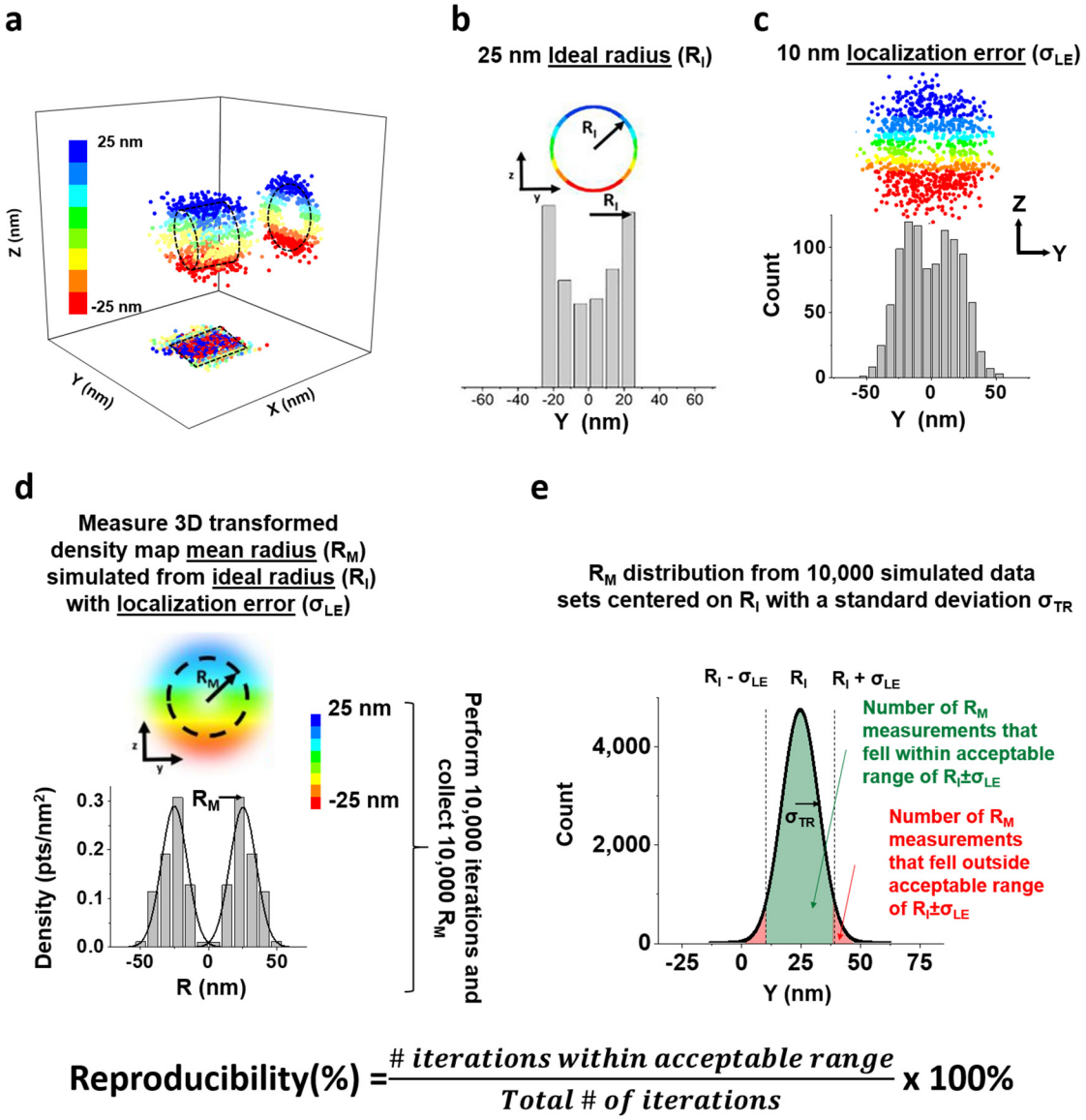

$$\text{Reproducibility(\%)} = \frac{\#\ iterations\ within\ acceptable\ range}{Total\ \#\ of\ iterations} \times 100\%$$

Supplementary Figure S15 Calculation of reproducibility percentage. **a.** Data sets were simulated in three dimensions. Color bar indicates z position of the simulated points. **b.** Each data set was simulated first with an ideal radius (R_I), which was 25 nm in this example. This represents the diameters allowed within the central channel of the NPC. For sub-regions within the cytoplasmic fibril radii between 25-110 nm was used. For nuclear basket radii of 25-100 was utilized to account for the larger freedom of movement allowed in those

sub-regions **c.** Subsequently, a localization error (σ_{LE}), 10 nm in this example, was added to each point. Using a 5-nm optimal bin size for demonstration, the 2D histogram of the simulated data set with a 25-nm radius and 10-nm localization precision was determined. **d.** 1,000 data sets were simulated with an ideal 25-nm radius (R_I) and a localization error (σ_{LE}) of 10 nm. The resultant 3D histograms were then each fitted with a Gaussian function to localize the mean position of each peak, which is designated as the mean radius (R_M). **e.** The histogram for all the R_M values was determined and two parameters were obtained: the reproducibility percentage and the standard deviation of the R_M peak fittings. **f.** For the reproducibility percentage, the number of simulated data sets that fell within the acceptable range of $R_I \pm \sigma_{LE}$ were counted. The acceptable range of $R_I \pm \sigma_{LE}$ was chosen because, in principle, the resolution of any two Gaussian fittings is limited to the standard deviation or spread of those peaks, which is due to the simulated localization error (σ_{LE}) in our simulation and contributed to by the single molecule localization error in our experiments. For the standard deviation of the peak fits, the term describes how wide the R_M peak fits were distributed and is designated as σ_{TR}. After 1,000 simulations, the histogram for R_M values converges on the mean (R_I) from which they were originally sampled, while the spread of the R_M histogram (σ_{TR}) converges on a value that is due to the number of simulated points in each distribution and simulated localization error. The figure was adapted from our previous publication with permission(8).

Supplementary Figure S15

Supplementary Table 1. Copies of nuclear basket FG-Nups determined by different methods in various cell lines

Nup153	Nup50	Tpr	Cell line	Mehods	Reference
8	32	16	Rat liver (lysis)	proteomics	(10)
32	16	32	HeLa, HEK293 (lysis)	proteomics	(11)
8	8	8	DLD-1 (live)	High-speed single-molecule microscopy & CRISPR/Cas9	Our result

Supplementary Table 1

Supplementary Table 2. The nuclear transport kinetics of mCherry-MCP-NLS only

	Export efficiency (%)	Export time (ms)	Frequency (events·(pore·s)$^{-1}$)
mCherry-MCP-NLS	2.7	3	4.48

Supplementary Table 2

Supplementary Table 3. Export time and efficiency of mRNA at various copies of Nup153

		Copy Number of Nup153-Nup50								
		0 (125 events)	1 (105 events)	2 (112 events)	3 (107 events)	4 (104 events)	5 (102 events)	6 (106 events)	7 (103 events)	8 (128 events)
Efficiency (%)	Successful Export	8.1	9.2	11.6	23.4	26.9	28.1	29.5	28.2	31.2
	Abortive Export at Nuclear Basket	71.7	71.3	58.9	29.9	29.8	21.5	19.3	22.6	16.0
	Abortive Export at Central Scaffold	15.1	14.2	22.3	32.7	16.4	32.6	33.6	31.8	36.0
	Abortive Export at Cytoplasmic Fibril	5.1	5.3	7.2	14.0	26.9	17.8	17.6	17.4	16.6
Export time (ms)	Successful Export	12.0 ± 2.0	11.0 ± 1.0	12.0 ± 2.0	12.0 ± 1.0	11.0 ± 2.0	12.0 ± 2.0	13.0 ± 1.0	13.0 ± 1.0	14.0 ± 2.0
	Abortive Export at Nuclear Basket	4.0 ± 2.0	5.0 ± 2.0	6.0 ± 1.0	5.0 ± 2.0	6.0 ± 1.0	5.0 ± 2.0	7.0 ± 2.0	6.0 ± 1.0	7.0 ± 1.0
	Abortive Export at Central Scaffold	8.0 ± 2.0	9.0 ± 1.0	10.0 ± 1.0	9.0 ± 2.0	10.0 ± 1.0	11.0 ± 1.0	10.0 ± 2.0	10.0 ± 1.0	11.0 ±1.0
	Abortive Export at Cytoplasmic Fibril	11.0 ± 2.0	11.0 ± 2.0	12.0 ± 1.0	12.0 ± 1.0	11.0 ± 2.0	12.0 ± 2.0	12.0 ± 1.0	11.0 ± 2.0	13.0 ±1.0

*Event denotes mRNP export event that mRNPs diffuse from nucleus into NPC and then diffuse into cytoplasm or back nucleus.

Supplementary Table 3

Supplementary Table 4. Entrance frequency of mRNA into the nuclear basket at various copies of Tpr

Copy Number (cells)	Tpr								
	0 (26)	1 (8)	2 (9)	3 (7)	4 (5)	5 (4)	6 (4)	7 (5)	8 (17)
Frequency (events·(pore·s)$^{-1}$)	0.3 ± 0.1	0.4 ± 0.1	0.5 ± 0.1	0.6 ± 0.2	0.8 ± 0.1	0.9 ± 0.1	1 ± 0.2	1.1 ± 0.1	1.2 ± 0.2

Supplementary Table 4

Supplementary Table 5 The reproducibility of 3D nuclear transport routes

		Axial dimension sub-regions (nm)	Points (exp.)	Radial peak(s) (exp., nm)	Localization precision (exp., nm)	Reproducibility (exp,. %)	Points for ~90% reproducibility (sim.)
mRNPs	Integral NPCs	Nuclear basket -100 to -20	524	39.5		100.0	75
		Central scaffold -20 to 20	447	19	12	85.3	700
		Cytoplasmic fibril 20 to 70	366	38		98.7	100
	ΔTpr NPCs	Nuclear basket -100 to -20	499	29.5		94.3	105
		Central scaffold -20 to 20	340	18.5	12	84.7	700
		Cytoplasmic fibril 20 to 70	243	39		97.4	100
	ΔNup153-Nup50 NPCs	Nuclear basket -100 to -20	198, 914	0, 63		93.0 , 100.0	110, 80
		Central scaffold -20 to 20	410	20.5	12	92.0	400
		Cytoplasmic fibril 20 to 70	244	37		99.0 %	80
	ΔNup50 NPCs	Nuclear basket	540	42	12	100.0 %	75

	-100 to -20					
	Central scaffold -20 to 20	440	19		85.0 %	650
	Cytoplasmic fibril 20 to 70	255	38.5		100.0 %	80
GFP	**Nuclear basket -100 to -20**	310	0	12	99.0 %	110
	Central scaffold -20 to 20	295	0		98.0 %	110
	Cytoplasmic fibril 20 to 70	286	0		99.0 %	110
TAP-p15	**Nuclear basket -100 to -20**	271	41	10	99.0 %	100
	Central scaffold -20 to 20	119	21		85.8 %	85
	Cytoplasmic fibril 20 to 70	203	40		98.6 %	90

In cases where there were two radial peaks in one axial sub-region, the point number attributed to each peak was estimated by multiplying the total number of points for the overall probability density distribution by the ratio of areas for each peak in that 3D distribution. The exp means the experimentally obtained data; The sim is the computational simulation.

Supplementary Table 5

Supplementary Table 6. The count of mRNAs obtained from smFISH experiment

Cell#	Luc			TFRC		
	Total	Nucleus	Cytoplasm	Total	Nucleus	Cytoplasm
1	10817	4358	6459	3555	1695	1860
2	14776	8887	5889	2151	865	1286
3	18202	9255	8947	2994	1348	1646
4	12994	5796	7198	2083	518	1565
5	16996	9570	7426	1476	475	1001
6	13449	7714	5735	2544	985	1559
7	9303	5944	3359	1834	794	1040
8	6502	2772	3730	1890	876	1014
9	7150	3718	3432	3203	1073	2130
10	12697	6315	6382	3112	1024	2088
Mean	12288	6433	5856	2484	965	1519
SD	3692	2263	1764	662	344	405

* Luc : luciferase mRNA, TFRC: Human transferrin receptor protein mRNA

Supplementary Table 6

Supplementary Movies

Movie 1 A typical successful single mRNP export event captured by high speed single-molecule SPEED microscopy. A single mCherry-tagged mRNP (red spot) started from the nucleus, interacted with NPC (green spot) and arrived in the cytoplasm. Numbers denote time in milliseconds. Bar: 1μm. C, cytoplasm; N, nucleus.

Movie 2 A typical abortive single mRNP export event. A single mCherry-tagged mRNP (red spot) started from nucleus, interacted with NPC (green spot) and returned to the nucleus. Numbers denote time in milliseconds. Bar: 1μm. C, cytoplasm; N, nucleus.

Movie 3 Rotational view of 3D export route for mRNPs in NPC with the presence of all BSK proteins in a half cut-away manner. C, cytoplasm; N, Nucleus. Color changes from yellow to red indicates density from low to high.

Movie 4 Rotational view of 3D export route for mRNPs in ΔTpr NPC in a half cut-away manner. C, cytoplasm; N, Nucleus. Color changes from yellow to red indicates density from low to high.

Movie 5 Rotational view of 3D export route for mRNPs in ΔNup153-50 NPC in a half cut-away manner. C, cytoplasm; N, Nucleus. Color changes from yellow to red indicates density from low to high.

Movie 6 Rotational view of 3D export route for mRNPs in ΔNup50 NPC in a half cut-away manner. C, cytoplasm; N, Nucleus. Color changes from yellow to red indicates density from low to high.

Movie 7 3D export route of mRNPs (blue) in NPC with the presence of all BSK proteins superimposed with TAP-P15's 3D faciliated diffusion route (red). Color changes from light to dark indicate density from low to high.

Movie 8 3D export route of mRNPs (blue) in ΔNup153 NPC superimposed with GFP's 3D passive diffusion route (green). Color changes from light to dark indicate density from low to high.

Reference

1. V. Aksenova *et al.*, Nucleoporin TPR is an integral component of the TREX-2 mRNA export pathway. *Nature communications* **11**, 1-13 (2020).
2. V. Aksenova *et al.*, Distinct Basket Nucleoporins roles in Nuclear Pore Function and Gene Expression: Tpr is an integral component of the TREX-2 mRNA export pathway. *BioRxiv*, 685263 (2019).
3. J. Ma *et al.*, High-resolution three-dimensional mapping of mRNA export through the nuclear pore. *Nature communications* **4**, 2414 (2013).
4. L.-C. Tu, M. Huisman, Y.-C. Chung, C. S. Smith, D. Grunwald, Deconstructing transport-distribution reconstruction in the nuclear-pore complex. *Nature structural & molecular biology* **25**, 1061-1062 (2018).
5. A. Ruba, J. Kelich, J. Ma, W. Yang, Reply to 'Deconstructing transport-distribution reconstruction in the nuclear-pore complex'. *Nature structural & molecular biology* **25**, 1062-1064 (2018).
6. J. Ma, A. Goryaynov, W. Yang, Super-resolution 3D tomography of interactions and competition in the nuclear pore complex. *Nature Structural and Molecular Biology* **23**, 239 (2016).
7. Y. Li, M. Tingey, A. Ruba, W. Yang, High-speed super-resolution imaging of rotationally symmetric structures using SPEED microscopy and 2D-to-3D transformation. *Nature Protocols* **16**, 532-560 (2021).
8. Y. Li, S. L. Junod, A. Ruba, J. M. Kelich, W. Yang, Nuclear export of mRNA molecules studied by SPEED microscopy. *Methods* **153**, 46-62 (2019).
9. A. Ruba, W. Luo, J. Kelich, W. Yang, Obtaining 3D Super-resolution Information from 2D Super-resolution Images through a 2D-to-3D Transformation Algorithm. *bioRxiv*, 188060 (2017).
10. J. M. Cronshaw, A. N. Krutchinsky, W. Zhang, B. T. Chait, M. J. Matunis, Proteomic analysis of the mammalian nuclear pore complex. *The Journal of cell biology* **158**, 915-927 (2002).
11. A. Ori *et al.*, Cell type-specific nuclear pores: a case in point for context-dependent stoichiometry of molecular machines. *Molecular systems biology* **9**, 648 (2013).